Original Article

JCBFM

Journal of Cerebral Blood Flow & Metabolism
0(0) 1–13

DOI: 10.1177/0271678X241270198
journals.sagepub.com/home/jcbfm
Sage

Multimodal and serial MRI monitors brain peri-hematomal injury and repair mechanisms after experimental intracerebral hemorrhage

Laurent Puy[1], Gregory Kuchcinski[1], Clémence Leboullenger[1,2], Florent Auger[1], Charlotte Cordonnier[1] and Vincent Bérézowski[1,3]

Abstract

The peri-hematomal area (PHA) emerges as a key but puzzling interface where edematous and neuroinflammatory events co-occur after intracerebral hemorrhage (ICH), while being considered either as deleterious or protective. We aimed at unraveling the pathogeny and natural history of PHA over time after experimental ICH. Male and female rats were longitudinally followed up to day 7 using multimodal brain MRI. MRI measures were compared to neuropathological and behavioural results. While the peak of PHA volume at day 3 was predictive for spontaneous locomotor deficit without sex-effect, its drop at day 7 fitted with locomotor recovery and hematoma resorption. The PHA highest water density was observed at onset despite microvascular hypoperfusion, taken over by blood-brain barrier (BBB) leakage at day 3. Water density dropped at day 7, when vascular integrity was normalized, and the highest number of reactive astrocytes, microglial cells, and siderophages found. This study shows that the PHA with edematous component is hematoma-driven at onset and BBB-driven at day 3, but this excess neuroinflammation enabled PHA volume reduction and significant hematoma resorption as soon as day 7. Therapeutic interventions should consider this pathogeny, and be monitored by multimodal MRI in preclinical ICH models.

Keywords

Cerebral edema, intracerebral hemorrhage, MRI, neuroinflammation, rodent model

Received 26 January 2024; Revised 27 May 2024; Accepted 16 June 2024

Introduction

Intracerebral hemorrhage (ICH) is associated with a high mortality and morbidity rates, and remains devoid of specific treatment. Therefore, a better understanding of its pathophysiology at all stages of the disease is needed.[1] The peri-hematomal area (PHA) emerged as a key interface in which in which deleterious (secondary brain tissue damage) and protective (hematoma resorption and tissue repair) events occur.[2,3] Recent data suggest that the extent of PHA influences the prognosis: for every ml increase in absolute volume, the odds of a poor functional outcome increase by 3%.[4] To become a therapeutic target, PHA needs to be better defined and monitored. In preclinical models, PHA represents a common feature of several pathophysiological pathways induced by the bleeding. Most of experimental models investigate changes in the PHA using ex vivo methods, hampering its monitoring in the same subject and its correlation with behavior. This might result in misleading interpretations when comes the time to assess treatment effect.

Advances in magnetic resonance imaging (MRI) allow the study of PHA in vivo from animals to

[1]Univ. Lille, Inserm, CHU Lille, U1172 - LilNCog - Lille Neuroscience & Cognition, Lille, France
[2]Univ. Lille, CNRS, Inserm, CHU Lille, Institut Pasteur de Lille, Lille, France
[3]UArtois, Lens, France

Corresponding author:
Charlotte Cordonnier, Univ. Lille, Inserm, CHU Lille, UMR-S1172 - LilNCog - Lille Neuroscience & Cognition, Lille, France.
Email: Charlotte.Cordonnier@univ-lille.fr

humans. Few preclinical studies have used MRI to quantify PHA volume, and current methods are mainly based on manual segmentation, with inherent bias. Beyond quantification, few clinical and preclinical studies used multimodal MRI to assess the complex nature of changes that occur within the PHA over time.[5–11] In several experimental models, PHA gathers distinct components observed at various time points after ICH (water density, water mobility, microvascular water mobility, microvascular integrity, tissue perfusion, and hemosiderin deposition) that have not yet been monitored concurrently in vivo. As the elucidation of pathogenic mechanisms and the test of potential therapies are the purpose of preclinical research, it appears crucial to assess the evolution of ICH-induced brain damage and repair in the same subject through clinically relevant MRI parameters.

Over a 7-day period, we used repeated multimodal MRI in healthy male and female ICH rats to characterize the early temporal evolution of PHA volume and components. In order to provide further insight into these MRI features, we concurrently investigated histological data and behavior.

Methods

Ethical aspects

All experiments were approved by the national Ethical Committee in Animal Experimentation (CEEA, Comité d'Ethique en Experimentation Animale), from the French Ministry for Education and Research (agreement number: APAFIS#14066-2018031312529642v3) and were performed in strict compliance with the European Union Directive 2010/63/EU. Experiments were reported in accordance with the ARRIVE guidelines for reporting experiments involving animals.[12]

Animals and study design

Twelve-week-old Wistar rats were used, and included both males (280 to 350 g) and females (220 to 300 g) to adhere to the standards of good practice in experimental research. We prospectively studied 230 animals: 156 in the ICH group (sex ratio 1:1) and 74 in the sham group (sex ratio 1:1). After surgery, rats were prospectively followed-up for seven days at three time-points: day 0 (D0 = 4 ± 2 hours post ICH), day 3 (D3) and day 7 (D7). Repeated behavioral and MRI measurements were performed in each rat at each time point. A quarter of the animals was euthanized for histological purposes at the end of each time point and the fourth quarter of animals were kept alive for further investigations that are out of the scope of the current study.

Intracerebral hemorrhage induction: the double injection of autologous blood

Animals were anesthetized with isoflurane (1.5% to 2%) through spontaneous respiration. Core temperature was maintained at 36°C to 37°C throughout all surgical procedures. A stereotaxic apparatus was used to position the tip of the needle (26 gauge) at coordinates 0.4 mm anterior, 3.2 mm lateral, and 5.8 mm deep relative to bregma through a 1-mm craniotomy. The ICH was produced by injection of 50 μL of fresh (non-heparinized) autologous whole blood into the right striatum at a constant rate of 8 μL/min. After a 10-minute break, other 50 μL of blood were infused at the same rate for a total of 100 μL. The needle was left in place for 10 minutes after the infusion and was then withdrawn and followed by closure of the incision with sutures.[13] Rats were randomly assigned to the sham group or ICH group. Sham operation was restricted to needle insertion.

MRI acquisition parameters. All rats underwent a 7-Tesla micro-MRI (7-Tesla; BioSpec 70/20, Bruker, Ettlingen, Germany). Animals were anesthetized with isoflurane (1.5% to 2%) through spontaneous respiration, and core temperature was maintained at 36°C to 37°C throughout all MRI procedures. A cylindrical emitter antenna with an inner diameter of 72 mm and a receiving surface head coil both allowed data recording. A birdcage radiofrequency coil and a surface coil were used for radiofrequency transmission and reception, respectively. A 3-plane scout imaging sequence was obtained at the start of each MRI session to reproducibly position the animal in the magnet. The following sequences were performed at each time point (D0, D3, D7) and for each rat:

Anatomic axial and coronal T2-weighted spin-echo sequences (repetition time/echo time [TR/TE] = 5000/77 ms, field of view [FOV] = 4 × 4 cm, matrix = 256 × 256, slice thickness = 1 mm, no gap, 20 slices); ***Multiecho T2 spin-echo relaxometry*** (TR/TE = 5000/7, 21, 35, 49 and 63 ms, FOV = 4 × cm, matrix = 256 × 256, slice thickness = 1 mm, no gap, 20 slices); ***Multiecho T2 gradient-echo*** (TR/TE = 800/3; 7; 11; 16; 20; 24; 28 and 32 ms, FOV = 4 × 4 cm, matrix = 256 × 256, slice thickness = 1 mm, no gap, 7 slices); ***Diffusion-weighted imaging with multi-b values*** (TR/TE = 3000/21.50 ms, b-values = 10, 20, 40, 60, 80, 100, 400, 600, 800 et 1000 s/mm2, FOV = 4 × 4 cm, matrix = 108 × 96, slice thickness = 1 mm, no gap, 7 slices); ***Flow sensitive alternating inversion recovery-echo planar imaging (FAIR-EPI) pulsed Arterial-spin labelling (PASL) sequence:*** (*inversion time [TI]* = 35, 100, 200, 300, 400, 500, 600, 700, 800, 900, 1000, 1100,

1200, 1300, 1400 and 1600 ms, FOV = 4 × 4 cm, matrix = 108 × 96, 1 slice).

Image processing and analysis. We defined three regions of interest (ROIs): (1) ICH core, (2) peri-hematomal area and (3) healthy contralateral striatal tissue.

ICH and PHA volume assessment. ICH and PHA volumes were semi-automatically segmented using Mango© software (University of Texas, USA). In Mango©, prior to any segmentation procedure, all T2-axial images underwent brightness/contrast enhancement using a contrast control tool to increase image quality and enhance background separation as much as possible. Thresholding was then applied, the values were automatically set (using the auto-threshold tool) to include only the regions having pixels with high intensity levels, that isolated ICH, PHA and normal parenchyma. Ellipsoid region of interest (ROI) of the contralateral striatum was then manually defined. Segmentations were independently performed by two experienced operators (L.P and F.A) with excellent interobserver agreement (r = 0.92 and 0.82 for ICH and PHA volumes respectively). Rats with initial ICH volume $<10\,mm^3$ were excluded to ensure that all animals had a significant lesion.

Multimodal PHA characterization. Beyond volumetric analysis, we aimed to investigate the biophysical properties of PHA using different sequences. All the parametric maps reconstructions and manual ROIs delineation were performed as detailed below with ParaVision5.1® (PV5.1) software (Bruker, Biospin, Germany). ROIs representing the PHA were first delineated from T2 sequence and then coregistered with other sequences with some manual adjustment if needed.

As the absolute values differ in each experimental setup, relative values were calculated for each MRI parameter. To do so, a ratio (r) was calculated between the value of the lesion side (ROI 1) and the healthy side of a corresponding mirror ROI (ROI2) in the contralateral striatum. For instance, the ratio (rADC) between the ADC value of the lesion side and the healthy side of a corresponding mirror ROI was calculated as $rADC = ADC_{roi1}/ADC_{roi2}$. We investigated five components of the PHA:

Calculation of T2 and T2: water density and hemosiderin deposition*

The T2/T2* relaxation times were calculated by fitting the T2/T2* signal decrease with a monoexponential function. The equation used was as follows:

$$S(TE) = S_0 \times e^{\left(\frac{-TE}{T2}\right)}$$

Where S_0 is the proton density and TE is the echo time. TE is expressed in milliseconds (ms)

Relaxation rates (R2 and R2*) were expressed in s^{-1} and calculated as follow:

$$R_2 = 1000/T2$$

$$R_2^* = \frac{1000}{T_2^*}$$

We quantified "water density" using R2.[14] rR2 values >1.1 and <0.9 were suggestive of a decrease and increase of water density. We quantified hemosiderin deposition using R2*: rR2* > 1.1 was suggestive of an increase in hemosiderin.[15,16]

Calculation of the apparent diffusion coefficient (ADC): parenchymal water mobility

We used ADC values (mm^2/s) from diffusion weighted imaging (DWI) sequence to investigate the water mobility in the brain parenchyma. ADC coefficient was calculated by fitting diffusion signal on a monoexponential curve. The exponential function used was the following:

$$S(b) = S_0 \times e^{(-b/ADC)}$$

where S_0 is the signal measured when b = 0, b is the so-called "b factor".[17] rADC >1.1 and < 0.9 were suggestive of vasogenic edema and cytotoxic edema respectively. Based on our preliminary analysis and previous clinical studies,[18] we hypothesized that both cytotoxic and vasogenic edema can occur concomitantly within the PHA. Hence, we used voxel-based approach rather than the absolute values of the ROI. To do so, we used the Paravision 5.1 software to estimate the number of voxels within ROIs and their respective grey level intensity and build a histogram to represent the distribution of grey level. The 95%IC distribution of voxel within the contralateral ROI was considered as the reference. We stratified voxels within PHA into three categories based on grey level distribution: voxels with ADC < 2.5th and > 97.5th percentile of contralateral voxels indicated hypoADC and hyperADC values, whilst voxels within the 95%IC range were considered normal. The percentage of each category was then calculated.

Calculation of the pseudo-diffusion coefficient (D): microvascular fluid mobility*

We used the DWI sequence to assess water mobility variations in the microvascular compartment within

the PHA. At low b values between 0 and 100 s/mm^2, the constraints of water molecules in the microvascular compartment can be evaluated quantitatively by calculating the pseudo-diffusive component D*.[19] The D* value was obtained from a bi-exponential equation according to Le Bihan[17] corrected and solved on GraphPad Prism (version 7.00 for Mac, GraphPad Software, La Jolla, CA, USA), as follows:

$$\frac{S}{S0} = (1-f).e^{-ADC.b} + f.e^{-(ADC+D^*).b}.e^{-\left(\frac{TE}{T2r}\right)}$$

In this formula, b is the diffusion coefficient, S is the signal measured for a value of b, S0 is the signal measured when b = 0, f is the fraction of the circulating blood volume fixed between 0 and 0.05%, and ADC is the apparent diffusion coefficient. TE is the echo time (21.50 ms), and T2r the relaxation of brain tissue without diffusion gradients (b = 0). Indeed, considering the edematous nature of PHA during ICH, relaxation times of brain tissue (T2) may have significant differences. We thus included a correction in the data analysis for low b values, the latter being sensitive to T2r. An illustration of b values decay curve is available in the supplementary Figure 1. Relative D* (rD*) values >1.1 were suggestive for an increased mobility of water molecules in the microvasculature referring to an increased microvascular patency or blood-brain barrier (BBB) leakage.[19] By contrast, relative D* values <0.9 were suggestive for a decreased mobility of water molecules in microvessels, referring to a decreased microvascular patency.

Calculation of the cerebral blood flow (CBF): brain tissue blood perfusion

The CBF was assessed using the FAIR PASL sequences.[20] PASL uses arterial blood water as an endogenous tracer by inverting the magnetization of the blood using radiofrequency pulses.

After a delay (TI: Inversion Time) allowing the labelled blood to flow into the brain tissue, "labelled" images were acquired. Separate "control" images were also acquired without prior labelling of arterial spins. The signal difference between "control" and "labelled" images provides a measure of labelled blood from arteries delivered to the tissue by perfusion. CBF calculation was performed using the following formula:

$$CBF = \lambda \times \frac{T1_{\text{control images}}}{T1_{blood}} \times \left(\frac{1}{T1_{\text{labeled images}}} - \frac{1}{T1_{\text{Control images}}}\right)$$

with T1 estimated as follows: TI: $S(TI) = S_0 \times \left[1 - 2e^{(-TI/T1)}\right]\left[+e^{(-TR/T1)}\right]$. Where λ is the blood-brain partition coefficient. In our experiences, T1blood and λ are equal respectively to 2400 ms and 0.9 mL/g. The unit of CBF is mL/100 g/min. Relative rCBF >1.1 and <0.9 were suggestive of hyper and hypo-perfusion. We hypothesized that both hypo- and hyperperfusion can occur concomitantly within the PHA. Hence, we used voxel-based approach with the same method described for ADC values.

Behavioral testing

Spontaneous locomotion. Spontaneous locomotor activity was automatically recorded using an infrared actimeter (Panlab, Bioseb, Vitrolles, France). The apparatus consisted of a square arena (45 cm in length, 45 cm in width and 35 cm in height) with a black polymethyl methacrylate floor and transparent 34-cm-high polymethyl methacrylate walls. Rats were placed in the center of the arena and allowed to explore freely for 10 min. Activity was recorded by two rows of infrared photocell sensors and processed with Actitrack software (Bioseb). The total distance covered (in cm), the number of rearings (n), the maximum speed recorded (Smax, in cm/second) and the duration of inactivity (resting time, in seconds) were collected at each time-point.[21]

Histopathological correlates: tissue characterisation, neuroinflammation and microvascular changes

At the end of the protocol, rats were euthanized with an overdose of pentobarbital (200 mg/kg, intraperitoneal). For tissue staining, rats were transcardially perfused with heparinized physiologic saline for 5 min and decapitated. Subsequently, brains were isolated and fixed in methacarn solution (60% methanol-30% chloroform-10% acetic acid) at 4°C for 1 day, then in 70% ethanol at 4°C for 1 day, followed by paraffin embedding. Brains were serially sliced at 5 µm thickness. All stainings and immunolabellings were performed on serial-sections of 5 µm each. Sections of formalin-fixed paraffin embedded tissue were stained routinely with hematoxylin–eosin (H&E) for the identification of ICH and structural analysis of the tissue. Perls' staining was done to screen for iron deposits using Tissue-Tek Prisma Plus automated Stainer (Sakura). Slides were placed in Potassium Ferricyanide solution (2% Potassium Ferricyanide – 25 ml and 2% Hydrochloric acid −25 ml) for 20 minutes, and then counterstained in Nuclear fast Red for 5 minutes, rinsed in distilled water, dehydrated and mounted.

We used Glial fibrillary acidic protein (GFAP) and ionized calcium-binding adapter molecule 1 (Iba1) immunolabelling to identify neuroinflammatory cells (active astrocytes and microglia respectively) within the PHA. These markers were immunolabelled using

a VENTANA BenchMark GX immunohistochemistry automated staining machine (Roche). The primary antibody was a rabbit polyclonal IgG (Ventana-Roche). We used the i-View DAB detection kit® (Ventana Medicals System, Roche Group) as an indirect biotin streptavidin system for the detection of the primary IgG antibody. Tissue sections were counterstained using bluing reagent solution (Ventana-Roche). The presence of GFAP was assessed by rabbit monoclonal primary antibody (Roche). The presence of Iba1 was assessed by a rabbit anti-mouse IgG antibody (1:500, Wako Chemicals USA, Richmond, VA, USA). Nucleated cells were stained green using a Methyl Green solution (H-3402, Vector Laboratories). For each immunostaining, a tissue section was processed identically except that the primary antibody was omitted as a specificity control and revealed no signal. A brightfield slide scanner (Zeiss Axioscan Z1) digitised the whole tissue section at 20-fold magnification after staining. Immunolabelled sections were independently analysed by two experienced operators (L.P and V.B). A staining surface ratio ([stacking surface/whole section surface]*10^3) was calculated with a semi-automated method using ImageJ software in order to quantify the positively stained or labelled surface in the PHA.

The fluorescence-based visualization of brain microvascular patency as well as BBB integrity was enabled by the observation of both distribution and extravasation of fluorescein isothiocyanate (FITC)-Dextran (2000 kDa, $10\,mg \cdot mL^{-1}$, Sigma-Aldrich, Saint-Quentin Fallavier, France) through patent microvessels. A 500 µL volume of FITC-Dextran in physiologic saline solution was injected into the caudal vein of rats. After 2 min, rats were decapitated. Brains were extracted, frozen in liquid nitrogen and stored at −80°C until use. Thirty micrometer-slices were coronally cut using a cryostat (Leika), and mounted with Vectashield hardset medium with DAPI (Vector Laboratories, Burlingame, CA, USA). The resulting slides were scanned in three dimensions using a slide scanner (Zeiss Axio Scan.Z1, Gena, Germany), and post-processed using a 3D data projection method that projects the voxels of maximum intensity of the different slices into a viewing plane (Maximum Intensity Projection).

Statistical analysis

Continuous variables are expressed as mean ± SD or median and interquartile range in cases of non-normal distribution. Normality of distribution was checked graphically and according to the Shapiro-Wilk test. Categorical variables are expressed as frequencies and percentages.

The 7-day evolution of MRI parameters (using ratio ROI1/ROI2 as a continuous variable) in ICH animals was assessed using a linear mixed model including time (as categorical variable) and sex (as adjustment factor) as fixed effect with an unstructured covariance pattern model to take into account the correlation between repeated measures within subjects. Normality of the model residuals was checked using Q-Q plots.

The 7-day evolution of locomotor performances was compared between the Sham and ICH animals by using linear mixed models (an unstructured covariance pattern model) to account for the correlation between repeated measures within subjects, and by including the time (as categorical variable), group and interaction term (group*time) as fixed effects. Sex was added as adjustment factor because the body surface area can influence automatic detection on the infrared actimeter platform. In case of significant interaction term, post-hoc comparisons within and between Sham and ICH animals (changes between each time point) were performed using linear contrast. A linear regression model (adjusted for sex) was used to assess the relation between PHA peak and locomotor performance. Correlation between MRI and histology findings were performed using the Pearson's correlation test. All statistical tests were 2-sided and a *p-value* of ≤ 0.05 was considered as statistically significant.

Results

Among the 156 ICH animals, 8 died before the first MRI and 19 had a baseline ICH volume $< 10\,mm^3$. Therefore, 74 shams and 129 ICH animals were included in the study.

Temporal assessment of ICH and PHA volumes

The natural history of ICH and PHA volumes assessed on T2 sequence are reported in Figure 1. In the ICH group, D0 hematoma mean volume was $22.28 \pm 9.4\,mm^3$ (Figure 1). The volume of ICH was similar between D0 and D3 and decreased significantly at D7 ($13.10 \pm 6.2\,mm^3$, $p < 0.0001$ with D0 as reference). This corresponded to a nearly 40% reduction of the ICH volume. In the ICH group, D0 PHA mean volume was $22.92 \pm 7.8\,mm^3$ (Figure 1). We observed the PHA volume peak at D3 ($25.23 \pm 10.1\,mm^3$; this corresponds to a 10% increase) and a dramatic decrease at D7 ($1.73 \pm 1.1\,mm^3$; $p < 0.001$ with D3 as reference).

Temporal assessment of changes occurring in the PHA

Water mobility: rADC was 0.95 ± 0.11, 1.26 ± 0.14 ($p < 0.0001$ with D0 as reference) and 1.08 ± 0.10 at D0, D3 and D7 respectively (Figure 2(a) and (b)).

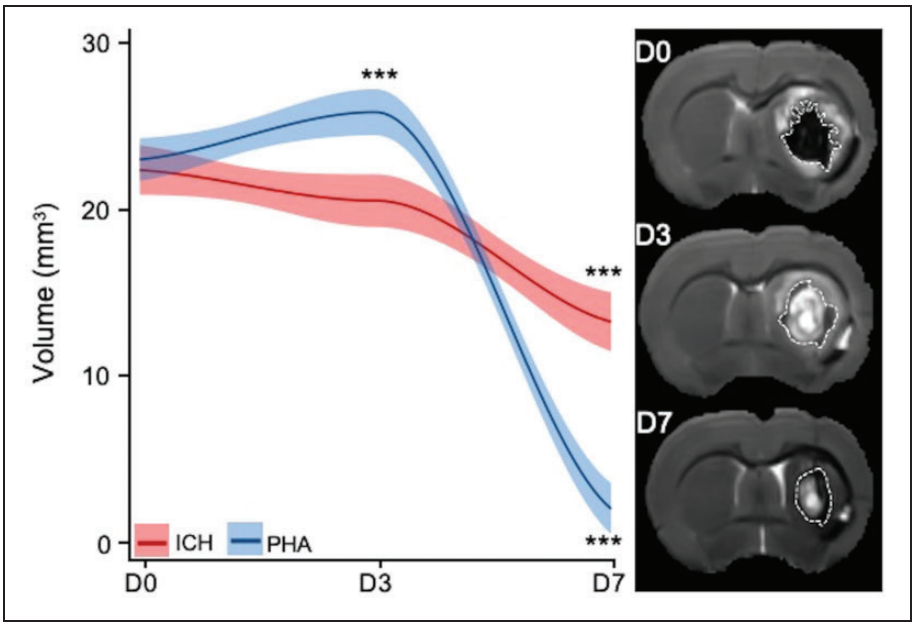

Figure 1. Temporal course of ICH and PHA volume in the acute phase. Temporal course of ICH and PHA volumes between day 0 and day 7. (***$p \leq 0.001$ with D0 as reference). Graphic built using a smooth local regression (http://www.r-project.org/, ggplot2 package, method ="loess"). On the left, brain MRI axial T2 image of an ICH rat. The MRI sequence is T2-weighted. The appearance of ICH on MRI depends mainly on the age of the hematoma and stage of erythrocyte- and hemoglobin degradation.[36] At D0, ICH core appears in hyposignal surrounded by a hyperintensity signal (PHA) within the right striatum. At D3, a hypersignal is observed in the center of the ICH, corresponding to a hemolysis process. At D7, ICH core is smaller, with ongoing hemolysis (hypersignal) surrounding by a hyposignal.[36] The dotted white circle delineates the ICH core. The adjacent hypersignal corresponds to the peri-hematomal edema. ICH = intracerebral hemorrhage, PHA = peri-hematomal area.

Voxel-based analysis of ADC showed both cytotoxic and vasogenic values at D0 (32% and 29% of cytotoxic and vasogenic voxels). At D3, PHA was mostly vasogenic (77% of voxels) (Figure 2(b)). At D7, 29% of voxel were still in vasogenic values.

Microvascular Water Mobility Assessment: rD* was 0.69 ± 0.23, 1.16 ± 0.14 ($p < 0.0001$ with D0 as reference) and 1.11 ± 0.12 at D0, D3 and D7 respectively (Figure 2(a)).

Tissue perfusion: rCBF was 0.50 ± 0.19, 1.06 ± 0.26 ($p < 0.0001$ with D0 as reference) and 1.10 ± 0.23 at D0, D3 and D7 respectively (Figure 2(a) and (b)). Voxel-based analysis of rCBF showed that PHA at D0 was mainly hypoperfused (40% and 3% of hypo and hyper-perfused voxels). We then observed at D3 and D7 a normalisation of CBF (>80% of voxels in normal values, with contralateral striatum as reference), even if some animals had a hyperperfused zone within their PHA at D3 (Figure 2(b)).

Water density: rR2 was minimal at D0 (0.70 ± 0.11), remained low but slightly increased at D3 (0.76 ± 0.09) and significantly increased at D7 (1.11 ± 0.09; $p < 0.0001$ with D3 as reference) (Figure 3(a)).

Hemosiderin deposition: rR2* was 1.70 ± 0.34 at D0, 1.45 ± 0.26 at D3 and peaked at D7 (2.11 ± 0.46; $p < 0.0001$ with D3 as reference) (Figure 3(a)).

Whatever the sequence, we did not find substantial changes in relative values in the sham group over time.

Histopathological correlates

Tissue characterisation with H&E and MSB stainings confirmed the presence of blood within the right striatum of ICH rats. The PHA was characterized by tissue pallor, that was maximal at D3. FITC-Dextran was used as a fluorescent tracer for assessing microvascular patency and integrity within the PHA (Figure 2(d)). At D0, we observed a dramatic decrease of positive microvascular signal without blur compared to sham, indicating a drop in microvascular patency at this stage of ICH. In contrast, at D3, the tracer was kept in the lumen of capillaries, which resulted in the detection of an intense fluorescent signal revealing tight vascular segments, but also diffused out of the capillaries, which were then surrounded by a blurred signal alongside the vascular segments (leaky capillaries). At D7, we observed a normalization of vascular patency although some leaky capillaries were still sparsely found in the PHA.

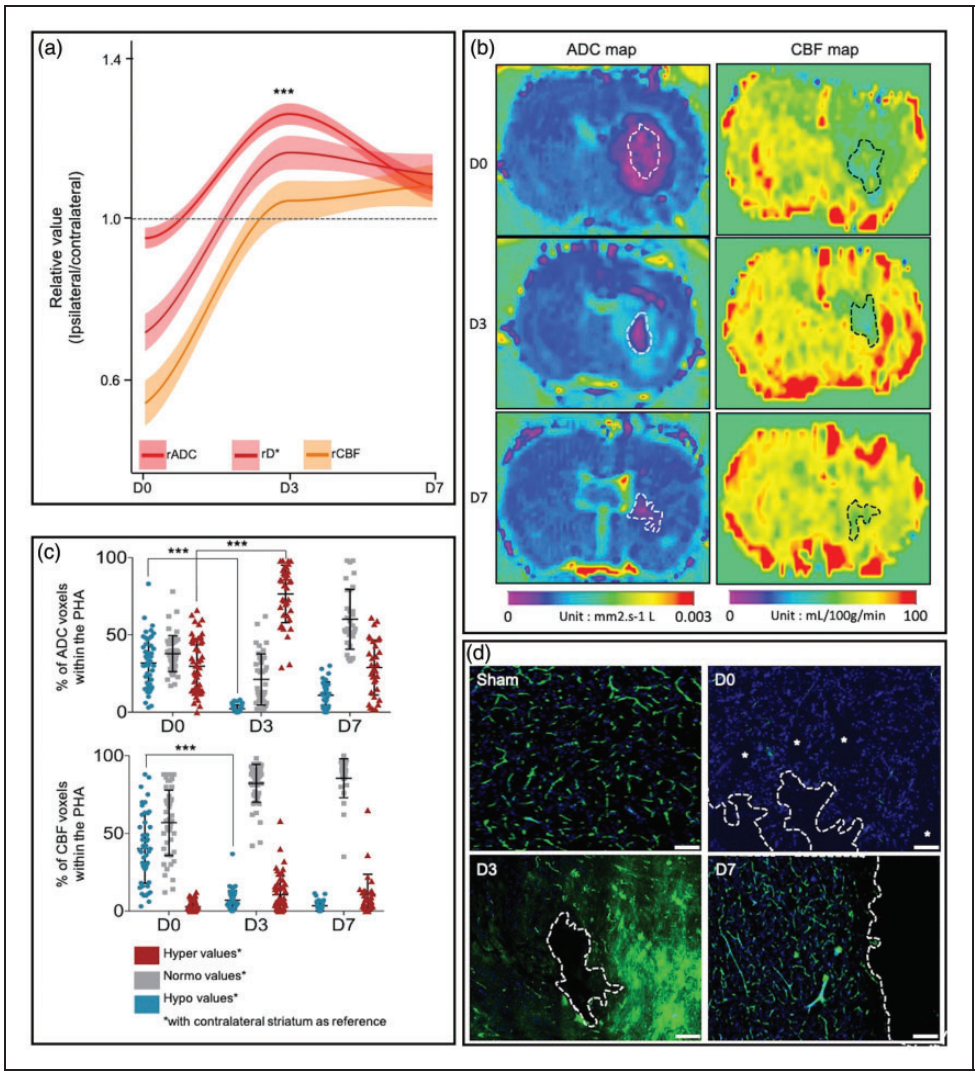

Figure 2. Water mobility, microvascular water mobility and tissue perfusion within the PHA. Temporal course between day 0 and day 7 of rADC (red line), rD* (purple-red line) and rCBF (orange line) values that indicate water mobility in brain tissue, water mobility in brain microvessels, and tissue perfusion within the PHA. The dotted grey line indicates a normal ratio value (= 1) (***$p \leq 0.001$, with D0 as reference). Statistical analysis was assessed using a linear mixed model including time (as categorical variable) and sex (as adjustment factor) as fixed effect. Graphic built using a smooth local regression (http://www.r-project.org/, ggplot2 package, method ="loess"). (B) Brain MRI of ADC and CBF mapping from DWI and PASL sequences at each timepoint. Warm colors (yellow to red) indicate higher ADC and CBF values and cool colors (blue) indicate lower values. The dotted white circle delineates the ICH core. Diffusion scale ranging from 0 to 0.003 mm^2 s^{-1} L and perfusion scale ranging from 0 to 100 mL/100 g/min. (C) Voxel-based analysis of ADC and CBF voxels within the PHA compared to contralateral striatum as reference. (D) Brain slices from fluorescein isothiocyanate (FITC)-Dextran-infused animals illustrate the different states of microvessel in the PHA. The blue-fluorescent DNA stain (DAPI; 4′,6-diamidino-2-phenylindole) corresponds to the presence of brain resident cells At D0, we observed a dramatic decrease of the microvessel density compared to sham, indicating a drop in microvascular patency at this stage of ICH. At D3, we observed an abundant leakage of the tracer resulting in an intense fluorescence signal. At D7, we observed a normalization of vascular integrity although some leaky capillaries were still sparsely found in the PHA. The dotted white circle delineates the ICH core and the asterisks indicate the presence of blood suffusion within the surrounding tissue. Scale bars = 50 μm. ICH = intracerebral hemorrhage. PHA = peri-hematomal area.

At D0, we did not observe any activated astrocyte (positive for GFAP) nor microglial cell (positive for Iba-1) within the PHA (all p = ns vs. sham, Figure 3 (b)). The expression of GFAP and Iba1 slightly increased from D3 (all $p < 0.01$ vs. D0 as reference, Figure 3(b)) and reached the peak at D7 (all $p < 0.0001$ vs. D0 as reference, Figure 3(b)). Perls' staining (indicative of iron deposition) showed a large number of iron-positive cells along the inner border of the hematoma from D3 but mostly at D7 (Figure 3(b)).

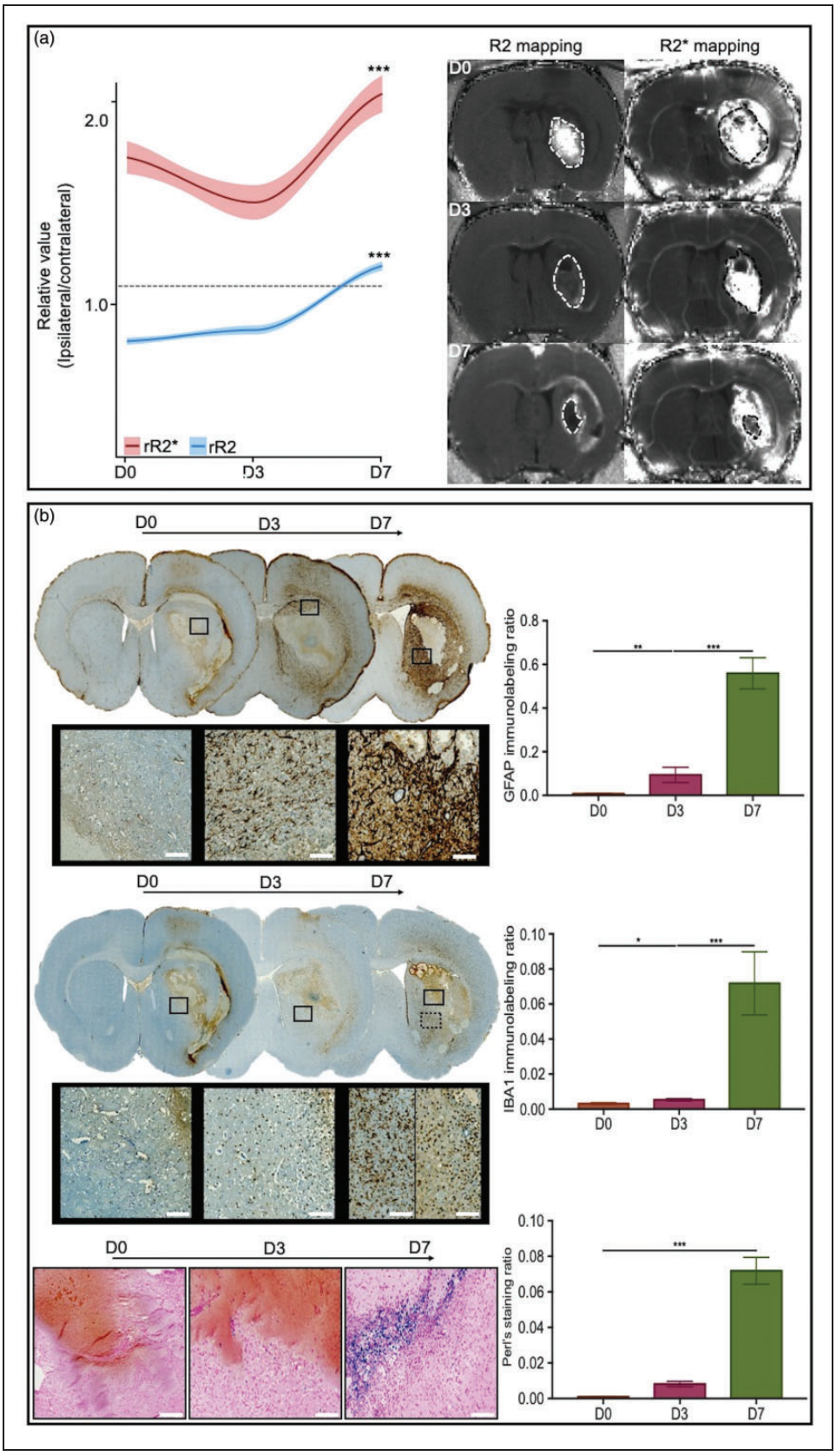

Figure 3. Water density, hemosiderin deposition and neuroinflammation within the PHA. (a) Temporal course of rR2 (blue line), indicating water density, and rR2* (red line) values, indicating of iron load between day 0 and day 7. The dotted grey line indicates a

Continued.

The sham animals did not exhibit significant astrocyte nor microglia activation (data not shown). The rR2* values were positively correlated with iron deposition from D3 to D7 ($r = 0.82$, p-value < 0.0001).

Spontaneous locomotor performances

Figure 4 shows the spontaneous locomotion of animals between day 0 and day 7. At day 0, ICH rats showed severe impairment affecting all the parameters of spontaneous locomotion: distance travelled (ICH group *vs* sham group, p-value: 989 ± 376 vs 2946 ± 255 cm, $p < 0.0001$), number of rearing (3[1–8] vs 56[38–67], $p < 0.0001$), maximum speed recorded (24 ± 7 vs 36 ± 5 cm/s, $p < 0.0001$) and resting time (432 ± 81 vs 262 ± 88 sec, $p < 0.0001$). At day 3, we observed a partial recovery in the ICH group that did not reach yet the sham's performances on three out of the four studied parameters: distance travelled (2875 ± 246 vs 3538 ± 176 cm, $p = 0.001$), number of rearing (31[17–55] vs 64[41–78], $p < 0.0001$) and maximum speed recorded (33 ± 6 vs 38 ± 5 cm/s, $p < 0.0001$). At day 7, ICH rats showed complete recovery of locomotor function (all p-value > 0.1 vs. sham). In multivariable regression model adjusted for sex, poorer spontaneous locomotor performances were associated with the peak of PHA volume at D3 ($p < 0.05$ for each parameter, see Table 1 for statistic details).

Discussion

Our study provides insights into the kinetics of injury and recovery processes following ICH by combining longitudinal multimodal MR imaging with both behavioral and histological investigations in a large cohort of healthy male and female ICH rats.

Although all rats experienced an initial sizable ICH and were severely injured, they spontaneously improved locomotion until complete recovery at D7. Active hematoma resorption (≈40% of the initial lesion) gradually occurs in those seven days after ICH, especially after D3, and might contribute to the recovery of neurological function.

In our study, all rats exhibited peri-hematomal hypersignal on T2 sequence as early as the first four hours after ICH induction, that was maximal at D3 and almost disappeared at D7. The peak of PHA volume was predictive for spontaneous locomotor deficit without sex-effect in adjusted analysis, and the decrease of PHA at D7 fitted with locomotor recovery.

To better understand the processes leading these lesions resorption (HIC and edema) and functional recovery, we aimed to characterize the longitudinal changes that occur within the PHA. The PHA is usually termed "peri-hematomal edema" in the literature, but our results suggest that this term does not reflect the full extent of the mechanisms at play.[22,23] We observed four distinct components, that contribute to the genesis of peri-ICH tissue injury and resolution: (1) water infiltration into the brain tissue; (2) microvascular changes; (3) activation and accumulation of inflammatory cells and (4) iron deposits. These components have their own kinetics, defining three critical phases of PHA natural history that may serve as endpoints for future experimental therapeutic studies: (i) a hyperacute phase of mass effect and tissue crush (4 hours), (ii) a pro-inflammatory induction phase (D3), and (iii) a phase of recovery (D7).

We first studied water density through the rR2 value that dropped within the first few hours. This early and massive water entry in the ICH surrounding tissue may be related to mechanical mass effect and extravasation of plasma proteins secondary to clot formation and retraction.[24,25] Of note, we observed a 10% mismatch at D3 between PHA volume, that peaked at D3, and water density, that tended to decrease, emphasizing that water (edema) is not the only component of PHA. At D7, we found an increase in rR2 values suggesting a drop in water content. However, the concurrent infiltration of inflammatory cells raises the possibility that R2 values reflect not only for the brain water content but

Figure 3. Continued.
normal ratio value (=1) (***$p \leq 0.001$, with D3 as reference). Statistical analysis was assessed using a linear mixed model including time (as categorical variable) and sex (as adjustment factor) as fixed effect. Graphic built using a smooth local regression (http://www.r-project.org/, ggplot2 package, method ="loess"). On the right, representative example of T2 relaxometry (R2) and T2* relaxometry (R2*) mappings obtain with 7-T MRI at each time-point. For R2 mapping, dark and white colors within the PHA indicate high and lower water density level within the PHA. By contrast, for R2* mapping, dark and white colors indicate low and high iron concentration level within the PHA. The dotted white circle delineates the ICH core and (b) brain slices from ICH animals euthanatized at D0, D3 and D7 immunolabelled for GFAP and Iba1 and stained for Perl's reaction indicating reactive astrocytes and microglia and iron deposits within the PHA. At D7, we observed two types of microglia: ramified (remotely from the PHA) and ameboid (at the border of ICH core). The graphs correspond to immunolabelling and staining ratio ([stacking surface/whole section surface] * 10^3) of GFAP, Iba1 and iron load within the PHA of $n = 8$ representative ICH rats (sex ratio 1:1). Bars and symbols correspond to the median value and the width of the 95% CI. Ratios were significantly different between time points according to Kruskal-Wallis followed by a Tukey *post hoc* test (***$p \leq 0.001$, **$p \leq 0.01$, *$p \leq 0.05$). Scale bars = 50 μm.

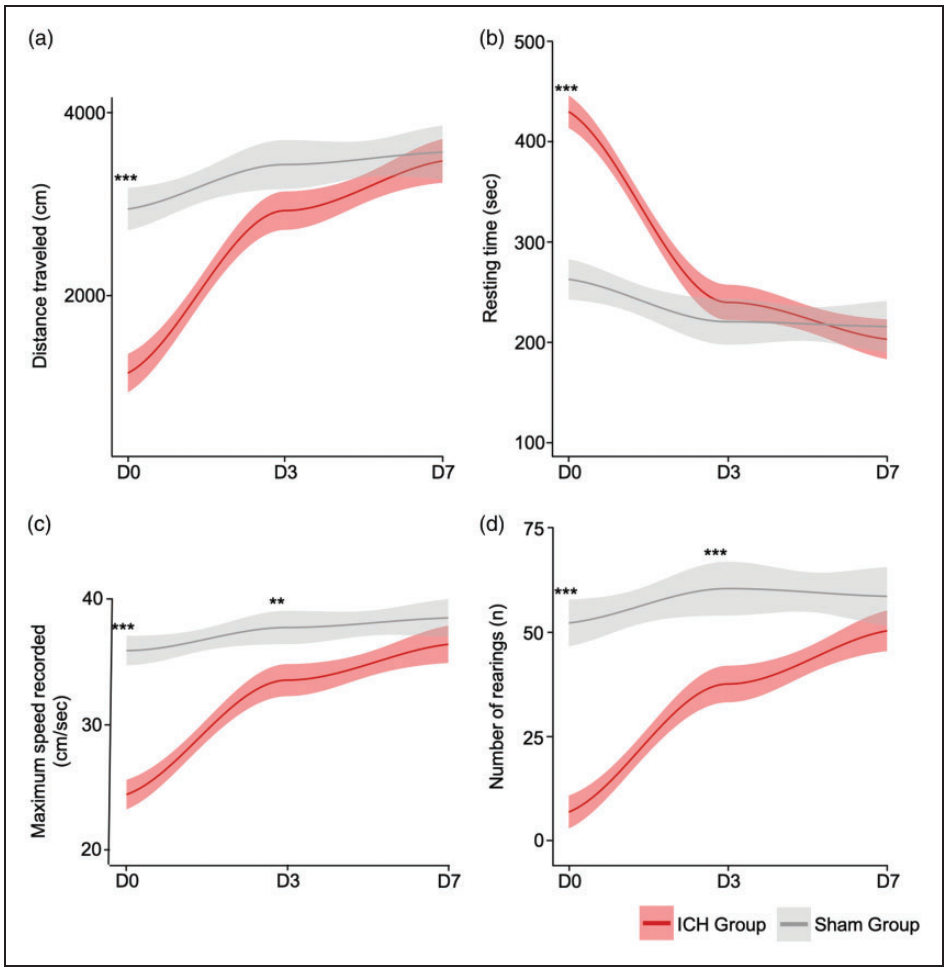

Figure 4. Spontaneous locomotion recovery in the acute phase. Traveled distance in cm (a), resting time in seconds (b), (c) maximum speed recorded in cm/seconde and (d) number of rearings. Measurements were assessed at day 0, day 3 and day 7. Red and grey lines correspond to the ICH groups and the sham groups performances respectively (***$p \leq 0.001$, **$p \leq 0.01$). Graphic built using a smooth local regression (http://www.r-project.org/, ggplot2 package, method ="loess").

Table 1. Association between PHA peak and spontaneous locomotion performances at D3.

Parameters	Estimates	p-values*
Distance traveled (cm)	−33.69	0.0061
Number of rearing (n)	−0.72	0.0089
Maximum speed (cm/sec)	−0.20	0.0013
Resting time (sec)	+2.66	0.0079

The statistical data comes from a multivariate regression model adjusted for sex. The PHA peak estimates suggest that for every 10 mm^3 increase in PHA volume, holding other predictor (sex) constant, one can expect a significant decrease of $-34*10=-340$; $-0.7*10=-7$ and $-0.2*10=-2$ in the distance traveled (cm), number of rearings (n) and maximum recorded speed (cm/sec), and an average increase of $+2.6*10=26$ seconds in the resting time.

also changes in the tissue structure surrounding ICH, including the infiltration of inflammatory cells.

We then monitored tissue water mobility (ADC), microvascular changes (D*) and perfusion (CBF). At D0, the mean rADC value was neither obviously increased, nor decreased. We therefore refined our method using voxel-based analysis and showed that both cytotoxic and vasogenic ADC values co-exist within the PHA during the hyperacute phase of ICH.[18]

This emphasizes the heterogeneous nature of PHA and tempers the predictive value of mean ADC value that is traditionally used in the literature. The use of voxel-based analysis is relevant to capture the co-occurrence of opposite (cytotoxic and vasogenic) values within the PHA. Whether cytotoxic edema and ischemia contribute to ICH pathology and prognosis remains controversial.[26–29] Our findings suggest a transient and reversible hypoperfusion at the microvascular level that did not reach the threshold of ischemia in our healthy rat brains. Indeed, within the first few hours, we observed a combination of hypoCBF and cytotoxic ADC on voxel-based analysis indicative of hypoperfusion. The concurrent low values of D* coefficient

within the PHA showed that this hypoperfusion occurred at the microvascular level. Those findings were supported by FITC-Dextran examination that showed a reduced detection of the flurorescent signal in microvessels, evidencing a drop in their patency. It suggests that this reversible hypoperfusion is related to the mass effect collapsing the microvessels in the vicinity of ICH. Importantly, longitudinal assessment showed a critical signal inversion of both ADC (almost 80% of voxel in vasogenic values), CBF and D* values at D3 with concurrent BBB leakage observed on FITC-Dextran sections. Therefore, our results didn't support the hypothesis of extended ischemia surrounding the ICH core[30,31] and confirmed the role of the BBB leakage, in the contribution of PHA growth at D3. This timepoint also marked the first observation of activated astrocytes and microglia within the PHA, initiating the neuro-inflammatory processes contributing to the hematoma resorption observed at D7.

As a marker of hematoma resolution, iron deposition was investigated using R2* map.[32] The massive entry of fresh blood was responsible for a diffuse blooming effect that artificially increased the rR2* value within the PHA at D0 (when no iron deposition was observed). We found a strong correlation between rR2* values and the extent of histological PHA iron deposits from D3 to D7. At D7, we observed hemosiderin deposition within the PHA with a close relationship between radiological and histological observations. The presence of inflammatory cells with scavenging activity and hemosiderin deposition in the PHA supports the role of this interface in the hematoma clearance process, as previously described in a human post-mortem study.[2]

We believe that R2* is a reliable marker to track in-vivo iron concentration within PHA to have an insight of hematoma resorption process and could also be used to monitor the effect of treatment targeting iron.

Our results are meaningful for translational researchers. Current emerging concepts in the field of ICH suggest that a use of sequential and complementary treatments is necessary to manage this complex disease. In this view, our multimodal approach emphasized day 3 as a key timepoint for sequential therapeutic intervention in ICH preclinical models. Before D3 therapeutic efforts should reduce the ICH-related injuries (e.g. mass effect, pro-inflammation), whilst after D3, they should enhance recovery process through modulation of neuroinflammation to ensure efficient hematoma resorption.

Most of current experimental studies investigate the PHA with methods that require animal euthanasia, excluding follow-up behavioral or tissue injury measurements in the same subject.

Ongoing research in ICH and the prospects of therapy have raised the need for a non-invasive method to investigate ICH in rodent models. Our volumetric measurements of PHA (peak at D3) were consistent with the literature in the field, which is mainly based on the dry/wet method.[23] We showed that a depiction of PHA components (microvessel injury, BBB disruption, neuroinflammation or iron deposits) is feasible *in vivo*: whatever the sequence studied, we found low standard deviations throughout our results. The consistent patterns of changes in these parameters and their correlation with terminal histological examinations promote the use of *in vivo* markers in experimental models. Monitoring these *in vivo* parameters after ICH may be useful for evaluating experimental therapies with longitudinal design. Importantly, all the MRI sequences described in this study are clinically relevant biomarkers: they are already used in human which facilitates the translational pipeline.[33,34]

Our study has some limits. We acknowledge that there may be partial volume bias in the volumetric analysis of the PHA, but the same semi-automatic segmentation method was used for all images, reducing the risk of bias in the statistical analysis. Our experimental ICH model used in these studies may not exactly mimic the clinical presentation of ICH, especially the vessel rupture and rebleeding phenomena. We used young healthy rats prone to effective resolution and functional recovery. One can speculate that in elderly patients, with comorbidities and chronic microangiopathy, the changes observed within the PHA could be amplified.

Our study has also strengths including the longitudinal design and the large sample size. Our MRI multimodal approach was strengthened by the use of semi-automated method for volume segmentation and the use voxel-based approach to better reflect the true nature of PHA. All our findings were supported by histopathological investigations. To minimize measurement bias and subjectivity of scales, we used fully automated method to assess spontaneous locomotion Finally, we included both male and female animals, in line with the 'Sex and Gender Equity in Research' guidelines.[35]

Conclusion

Our study demonstrates that PHA is more than just edema, but a highly dynamic interface between the hematoma and the brain tissue. Deleterious mechanisms take place in the PHA as well as endogenous repair mechanisms, which should be targeted within day 3 to prevent complications and ensure a switch to recovery. Multimodal MRI clearly appears as a reliable tool to track the progression of peri-hematomal changes (water density, microvascular changes, neuroinflammatory cells infiltration and iron deposition)

that should be widely used to monitor therapeutic interventions in translational ICH research.

Data availability

All data relevant to the study are included in the article. Data are available upon reasonable request.

Funding

The author(s) disclosed receipt of the following financial support for the research, authorship, and/or publication of this article: This work was supported by the Fondation Recherche sur les Accidents Vasculaires Cérébraux (project FRAVC 180713012), the Fondation pour la Recherche Médicale (FDM201806006375, fellowship L.P) and the Fondation I-SITE ULNE (fellowship L.P).

Acknowledgements

We warmly thank Nicolas Durieux (Univ. Lille, Inserm, CHU Lille,) for their great technical assistance in MRI acquisitions. We Thank Charlotte Laloux for assistance in the behavioral exploration platform for rodent (Federation of Neurosciences, University of Lille).

Declaration of conflicting interests

The author(s) declared the following potential conflicts of interest with respect to the research, authorship, and/or publication of this article: G.K, C.L, F.A, V.B: none.
L.P declares the following type of interests: speaker fees (Novonordisk).
C.C declares the following type of interests: speaker fees (Bristol-Myers Squibb); international RCT Steering committees for Biogen and Bayer.

Authors' contributions

L.P, V.B and C.C contributed to the conception and design of the study; L.P, G.K, C.L and F.A contributed to the acquisition and analysis of the data; L.P, G.K, C.L, V.B and C.C drafted the text and prepared the figures; all authors provided a review of the manuscript.

Supplementary material

Supplemental material for this article is available online.

ORCID iD

Laurent Puy https://orcid.org/0000-0002-9772-5192

References

1. Puy L, Parry-Jones AR, Sandset EC, et al. Intracerebral haemorrhage. *Nat Rev Dis Primers* 2023; 9: 14.
2. Puy L, Perbet R, Figeac M, et al. Brain peri-hematomal area, a strategic interface for blood clearance: a human neuropathological and transcriptomic study. *Stroke* 2022; 53: 2026–2035.
3. Garton T, Keep RF, Hua Y, et al. CD163, a hemoglobin/haptoglobin scavenger receptor, after intracerebral hemorrhage: functions in microglia/macrophages versus neurons. *Transl Stroke Res* 2017; 8: 612–616.
4. Cliteur MP, Sondag L, Cunningham L, et al. The association between perihaematomal oedema and functional outcome after spontaneous intracerebral haemorrhage: a systematic review and meta-analysis. *Eur Stroke J* 2023; 8: 423–433.
5. Qureshi AI, Wilson DA, Hanley DF, et al. No evidence for an ischemic penumbra in massive experimental intracerebral hemorrhage. *Neurology* 1999; 52: 266–272.
6. Orakcioglu B, Becker K, Sakowitz OW, et al. Serial diffusion and perfusion MRI analysis of the perihemorrhagic zone in a rat ICH model. *Acta Neurochir Suppl* 2008; 103: 15–18.
7. Orakcioglu B, Fiebach JB, Steiner T, et al. Evolution of early perihemorrhagic changes – ischemia vs. edema: an MRI study in rats. *Exp Neurol* 2005; 193: 369–376.
8. Knight RA, Han Y, Nagaraja TN, et al. Temporal MRI assessment of intracerebral hemorrhage in rats. *Stroke* 2008; 39: 2596–2602.
9. Huang L-C, Liew H-K, Cheng H-Y, et al. Brain magnetic resonance imaging of intracerebral hemorrhagic rats after alcohol consumption. *J Stroke Cerebrovasc Dis* 2018; 27: 3493–3502.
10. Yang D, Knight RA, Han Y, et al. Statins protect the blood brain barrier acutely after experimental intracerebral hemorrhage. *J Behav Brain Sci* 2013; 3: 100–106.
11. Yang J, Li Q, Wang Z, et al. Multimodality MRI assessment of grey and white matter injury and blood-brain barrier disruption after intracerebral haemorrhage in mice. *Sci Rep* 2017; 7: 40358.
12. Percie Du Sert N, Hurst V, Ahluwalia A, et al. The ARRIVE guidelines 2.0: updated guidelines for reporting animal research. *PLoS Biol* 2020; 18: e3000410.
13. Deinsberger W, Vogel J, Kuschinsky W, et al. Experimental intracerebral hemorrhage: description of a double injection model in rats. *Neurol Res* 1996; 18: 475–477.
14. Cheng H-LM, Stikov N, Ghugre NR, et al. Practical medical applications of quantitative MR relaxometry. *J Magn Reson Imaging* 2012; 36: 805–824.
15. Haque ME, Gabr RE, Zhao X, et al. Serial quantitative neuroimaging of iron in the intracerebral hemorrhage pig model. *J Cereb Blood Flow Metab* 2018; 38: 375–381.
16. Wei J, Novakovic N, Chenevert TL, et al. Perihematomal brain tissue iron concentration measurement by MRI in patients with intracerebral hemorrhage. *CNS Neurosci Ther* 2020; 26: 896–901.
17. Le Bihan D. The 'wet mind': water and functional neuroimaging. *Phys Med Biol* 2007; 52: R57–90.
18. Tsai Y-H, Hsu L-M, Weng H-H, et al. Voxel-based analysis of apparent diffusion coefficient in perihaematomal oedema: associated factors and outcome predictive value for intracerebral haemorrhage. *BMJ Open* 2011; 1: e000230.
19. Kuntz M, Mysiorek C, Pétrault O, et al. Stroke-induced brain parenchymal injury drives blood-brain barrier early leakage kinetics: a combined in vivo/in vitro study. *J Cereb Blood Flow Metab* 2014; 34: 95–107.

20. Wang DJJ, Alger JR, Qiao JX, et al. The value of arterial spin-labeled perfusion imaging in acute ischemic stroke: comparison with dynamic susceptibility contrast-enhanced MRI. *Stroke* 2012; 43: 1018–1024.
21. Puy L, Leboullenger C, Auger F, et al. Intracerebral hemorrhage-induced cognitive impairment in rats is associated with brain atrophy, hypometabolism, and network dysconnectivity. *Front Neurosci* 2022; 16: 882996.
22. Keep RF, Hua Y and Xi G. Intracerebral haemorrhage: mechanisms of injury and therapeutic targets. *Lancet Neurol* 2012; 11: 720–731.
23. Zheng H, Chen C, Zhang J, et al. Mechanism and therapy of brain edema after intracerebral hemorrhage. *Cerebrovasc Dis* 2016; 42: 155–169.
24. Xi G, Wagner KR, Keep RF, et al. Role of blood clot formation on early edema development after experimental intracerebral hemorrhage. *Stroke* 1998; 29: 2580–2586.
25. Wagner KR, Xi G, Hua Y, et al. Lobar intracerebral hemorrhage model in pigs: rapid edema development in perihematomal white matter. *Stroke* 1996; 27: 490–497.
26. Pascual AM, López-Mut JV, Benlloch V, et al. Perfusion-weighted magnetic resonance imaging in acute intracerebral hemorrhage at baseline and during the 1st and 2nd week: a longitudinal study. *Cerebrovasc Dis* 2007; 23: 6–13.
27. Stösser S, Neugebauer H, Althaus K, et al. Perihematomal diffusion restriction in intracerebral hemorrhage depends on hematoma volume, but does not predict outcome. *Cerebrovasc Dis* 2016; 42: 280–287.
28. Olivot J-M, Mlynash M, Kleinman JT, et al. MRI profile of the perihematomal region in acute intracerebral hemorrhage. *Stroke* 2010; 41: 2681–2683.
29. Gass A. Is there a penumbra surrounding intracerebral hemorrhage? *Cerebrovasc Dis* 2007; 23: 4–5.
30. Powers WJ, Zazulia AR, Videen TO, et al. Autoregulation of cerebral blood flow surrounding acute (6 to 22 hours) intracerebral hemorrhage. *Neurology* 2001; 57: 18–24.
31. Zazulia AR, Diringer MN, Videen TO, et al. Hypoperfusion without ischemia surrounding acute intracerebral hemorrhage. *J Cereb Blood Flow Metab* 2001; 21: 804–810.
32. Chaudhary N, Pandey AS, Griauzde J, et al. Brain tissue iron quantification by MRI in intracerebral hemorrhage: current translational evidence and pitfalls. *J Cereb Blood Flow Metab* 2019; 39: 562–564.
33. Second HEADS Roundtable Participants. Recommendations for clinical trials in ICH: the second hemorrhagic stroke academia industry roundtable. *Stroke* 2020; 51: 1333–1338.
34. Withers SE, Parry-Jones AR, Allan SM, et al. A Multi-Model pipeline for translational intracerebral haemorrhage research. *Transl Stroke Res* 2020; 11: 1229–1242.
35. Heidari S, Babor TF, De Castro P, et al. Sex and gender equity in research: rationale for the SAGER guidelines and recommended use. *Res Integr Peer Rev* 2016; 1: 2.
36. Parizel PM, Makkat S, Van Miert E, et al. Intracranial hemorrhage: principles of CT and MRI interpretation. *Eur Radiol* 2001; 11: 1770–1783.